



Original Research

Microstructure and mechanical properties of additive manufactured porous Ti–33Nb–4Sn scaffolds for orthopaedic applications

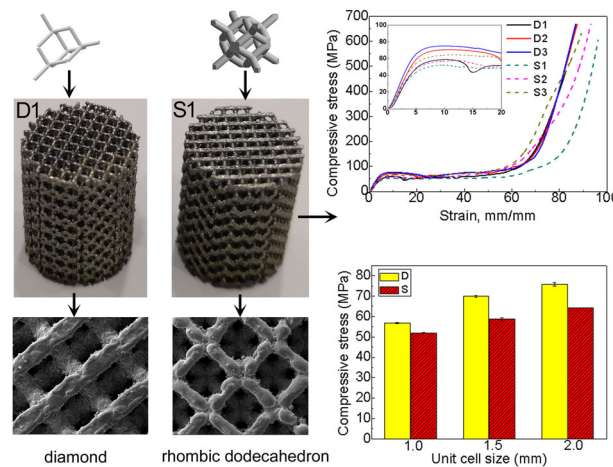
Xiaofan Cheng¹ · Shichao Liu¹ · Chao Chen¹ · Wei Chen¹ · Min Liu¹ · Ruidi Li¹ · Xiaoyong Zhang¹ · Kechao Zhou¹

Received: 14 June 2019 / Accepted: 17 July 2019 / Published online: 6 August 2019
© Springer Science+Business Media, LLC, part of Springer Nature 2019

Abstract

Customized porous titanium alloys have become the emerging materials for orthopaedic implant applications. In this work, diamond and rhombic dodecahedron porous Ti-33Nb-4Sn scaffolds were fabricated by selective laser melting (SLM). The phase, microstructure and defects characteristics were investigated systematically and correlated to the effects of pore structure, unit cell size and processing parameter on the mechanical properties of the scaffolds. Fine β phase dendrites were obtained in Ti-33Nb-4Sn scaffolds due to the fast solidification velocity in SLM process. The compressive and bending strength of the scaffolds decrease with the decrease of strut size and diamond structures showed both higher compressive and bending strength than the dodecahedron structures. Diamond Ti-33Nb-4Sn scaffold with compressive strength of 76 MPa, bending strength of 127 MPa and elastic modulus of 2.3 GPa was achieved by SLM, revealing the potential of Ti-33Nb-4Sn scaffolds for applications on orthopaedic implant.

Graphical Abstract



1 Introduction

With the process of entering the aging society, medical field desires for high quality load-bearing implants due to more and more people being suffering from bone diseases [1]. Among the numerous biomaterials for implants application, titanium alloys have become the most widely applied materials due to several advantages, such as high specific strength, high corrosion resistance and excellent biocompatibility [2]. As a widely used implant materials, Ti-6Al-4V alloys take advantages in high strength and

✉ Chao Chen
pkhqchenchao@126.com
✉ Xiaoyong Zhang
zhangxiaoyong@csu.edu.cn

¹ State Key Laboratory of Powder Metallurgy, Central South University, Changsha 410083, China

corrosion resistance [3], however, some drawbacks limit its application on medical implant fields. For example, the toxic elements such as vanadium and aluminium will cause side effects such as Alzheimer's disease and neuropathy [4]. Besides, the Young's modulus of Ti-6Al-4V is around ten times over that of the human bones, which may lead to mismatch in stiffness between an implant and the surrounding bone. And such mismatch can cause "stress shielding", which results in the reduction of stress transferred to adjoining bone, consequently leading to undesirable bone resorption [5–8]. Recently, Ti-Nb-Sn alloys have been verified as an emerging class of metastable β alloys proposed for orthopaedic applications [9–11]. It has been reported that the Ti-(30–35)Nb-(2–8)Sn (wt.%) is the range of commonly investigated composition for orthopaedic applications [12–15]. Guo et al. fabricated a metastable β -type Ti-33Nb-4Sn (wt.%) alloy with ultralow Young's modulus (36 GPa, versus ~30 GPa for human bone) and high ultimate strength (853 MPa) by cold rolling and annealing [16]. In our previous work, a metastable β -type Ti-37Nb-6Sn (wt.%) alloy with Young's modulus of 66 GPa, ultimate strength of 891 MPa and elongation of 27.5% was also manufactured by selective laser melting (SLM) [17].

Compared with natural bone tissue, the modulus of block Ti-Nb-Sn alloys was still unsatisfactory. One common method to reduce the modulus is to introduce porous structure [18–21]. Besides, the standard off-the-shelf block orthopaedic implants were hard to provide acceptable clinical solution due to geometrical complexity of natural bone tissues. Fortunately, the additive manufacturing (AM) technique, including SLM and electron beam melting (EBM), have capability to build complex porous patient-specific structures [22]. As a powder-based, layer-additive manufacturing technology, SLM can facilitate the manufacture of parts with almost no geometric constraints and is economically feasible for industrial production by using a high-intensity laser beam [23, 24]. Such AM technique is capable of manufacturing those implants with porous structures and optimized properties [25, 26]. The powder distribution, laser strategy and porosity are profound characteristics for titanium alloy porous implants to achieve qualified clinical outcomes [27]. Some works have been performed to demonstrate energy input parameters [28] and scan speed [29] can influence the mechanical properties of porous titanium parts through changing pores distribution and struts size.

For the practical application of the SLM-fabricated porous scaffolds, more works are needed to explore the effects of structural features such as pore structures, unit cell size and pore interconnectivity on the mechanical properties. In this work, porous Ti-33Nb-4Sn (wt.%) alloys scaffolds with porosity of 70% were fabricated by SLM. In terms of pores structure, two common types of structure were considered, the diamond structure and dodecahedron structure.

The phase and strut dimension were determined. The microstructure, defects and strut surface morphology were characterized. The effect of pores structure and struts size on the performance of metallic implants were investigated.

2 Materials and methods

2.1 Powder material preparation

Pure Ti and Sn powders were prepared by gas-phase atomization comprised spherical particles with average sizes of 21.7 and 8 μm , respectively (Fig. 1a, c). Pure Nb powders were prepared by mechanical crushing contained irregularly shaped particles with an average size of 30.5 μm (Fig. 1b). The microstructure of these three powders is shown in Fig. 1. These three powders were mixed by ball milling with weight proportion of 63:33:4 (Ti:Nb:Sn). Wearable Nylon ball mill jar and zirconia grinding ball were used to process powders. In order to get optimal milling powders, argon was selected as protective atmosphere and ball/powder ratio was defined as 2:1. Moreover, in case hazards caused by crushed powders occur during milling powders, the milling time and speed were selected as 12 h and 50 r/min, respectively. Finally, the Ti-33Nb-4Sn powders were evenly mixed (Fig. 1d), with a nominal particle size distribution between 11.1 and 56.9 μm and the median diameter (d_{50}) of 29.7 μm (Fig. 1e).

2.2 Selective laser melting process

SLM processing was performed using a Farsoon 271M instrument employing a standard alternating X/Y raster scanning strategy. Once layer n was completed, the bidirectional scanning of the next layer ($n + 1$) was performed after rotation by 67°. Prior to build samples, the chamber was purged with high purity argon until the oxygen content was <0.1% to minimize oxygen contamination. The laser wavelength was 1.06 μm with a spot size of 130 μm . The laser scanning speed was 1200 mm/s, and the power was 225 W, which have been proved by a series of orthogonal experiments to result in the best properties. The powder layer thickness was kept constant at 30 μm and the hatch distance was at 50 μm , while the substrate plate was heated to 200 °C.

2.3 Porous samples preparation

The three-dimensional (3D) computer aided design (CAD) model of the single unit cell created by Magics software is shown in Fig. 2. One is diamond structure (Fig. 2a) and another is the rhombic dodecahedron structure (Fig. 2b). The porosity of all samples is 70% while each type of

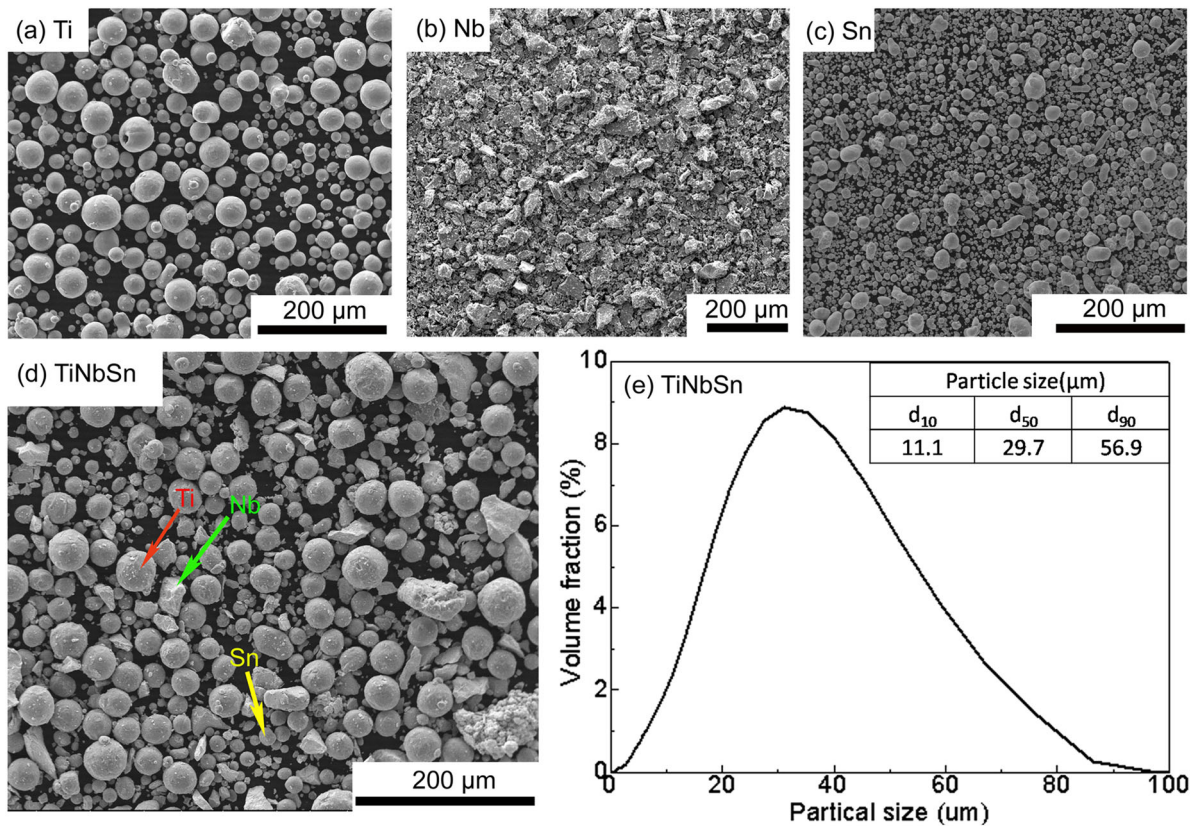


Fig. 1 Morphology of **a** Ti, **b** Nb, **c** Sn, and **d** mixed Ti-33Nb-4Sn powders. **e** Particle size distribution of the mixed Ti-33Nb-4Sn powders

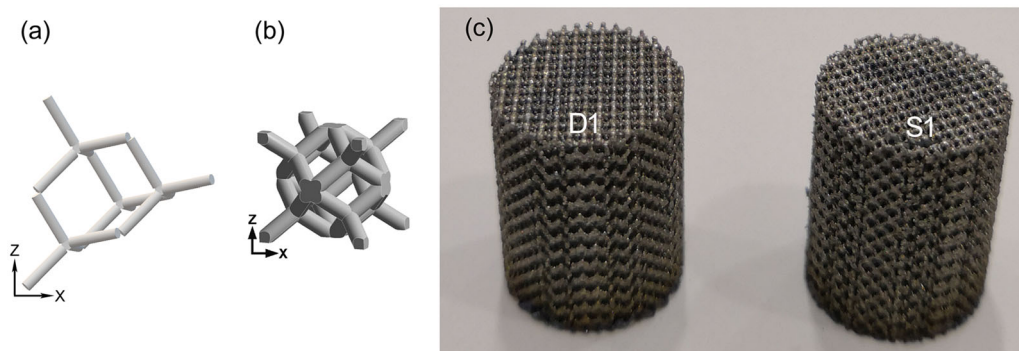


Fig. 2 The single unit cell of **a** diamond and **b** rhombic dodecahedron modelling. **c** Optical image of D1 and S1 produced by SLM

structure was divided as three different unit cell sizes, $1.0 \times 1.0 \times 1.0$ mm, $1.5 \times 1.5 \times 1.5$ mm and $2.0 \times 2.0 \times 2.0$ mm, respectively. Figure 2c shows the optical image of D1 and S1 produced by SLM. All the details of pore structure are listed in Table 1.

2.4 Microstructure and mechanical properties characterization

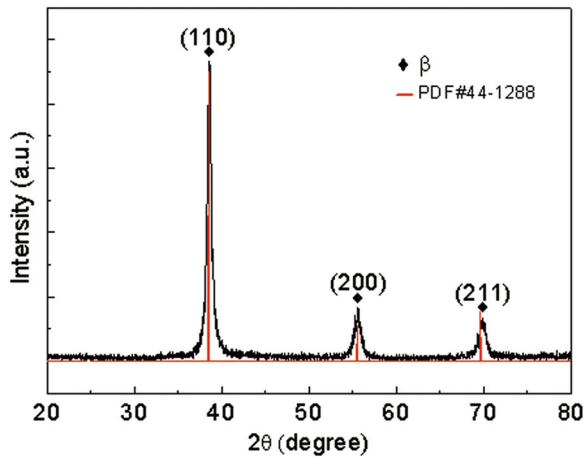
Six groups of porous samples were fabricated by SLM and then were separated from the building platform in the X-Y

plane by wire cutting. The residual powders inside the holes of porous samples were cleaned by high pressure air gun following by ultrasonic shock washing. Samples were embedded in resin, cut, ground and polished, similar to a typical metallographic preparation. SEM samples were etched using Kroll's Reagent (5 vol% HF, 10 vol% HNO₃, and 85 vol% H₂O) for 10 s.

The microstructures and surface topography were performed by scanning electron microscopy (SEM, JSM-6360LV, Japan). Phase analysis was performed using an X-ray diffractometer (XRD; Bruker D8 Discover 2500).

Table 1 Detail parameters for the designed specimens

Set number	Pore structure	Designed porosity (%)	Designed unit cell size (mm)	Designed strut size (mm)	Designed pore size (mm)
D1	Diamond	70	1.0 × 1.0 × 1.0	0.267	0.448
D2	Diamond	70	1.5 × 1.5 × 1.5	0.402	0.665
D3	Diamond	70	2.0 × 2.0 × 2.0	0.535	0.885
S1	Dodecahedron	70	1.0 × 1.0 × 1.0	0.192	0.512
S2	Dodecahedron	70	1.5 × 1.5 × 1.5	0.288	0.785
S3	Dodecahedron	70	2.0 × 2.0 × 2.0	0.384	1.040

**Fig. 3** XRD patterns of the SLM-produced Ti-33Nb-4Sn sample in the as-fabricated condition

According to ASTM E9-09 (2018), six groups cylindrical porous samples ($\phi 10$ mm × 13 mm) and cuboid-shaped porous samples (5 mm × 5 mm × 30 mm) were fabricated to use for compressive strength test and elastic modulus test respectively. Based on ASTM E855-08(2013), six groups cuboid-shaped porous samples (30 mm × 12 mm × 6 mm) were fabricated for bending test. Instron 3369 mechanical testing machine (America) was used in compressive strength test at strain rate of 0.5 mm/min and bending test at blend rate of 1 mm/min. The real porosity was measured by Automatic Density Analyzer (Quantachrome instruments corporation) via Testing of rigid cellular plastics method (ASTM B923-10). The real strut size was measured from SEM images. Then, the fracture surfaces of the bending tested samples were observed through SEM.

3 Results

3.1 Phase analysis and microstructure

Figure 3 shows the XRD patterns of SLM-fabricated porous samples. In the XRD patterns, three peaks were detected at

$2\theta = 38.5, 55.5,$ and 69.6° corresponding to (110), (200) and (211) planes of titanium alloy respectively, which indicates the presence of a single β -Ti phase. Because of the rapid solidification in SLM processing, the content of β -phase-stabilizing element (Nb) is relatively high leading to formation of undercooling β phase. However, the fast solidification restricts the precipitation of α phase. Therefore, only single β phase was observed [26]. Compared with PDF#44-1288, no mismatch in location and intensity of these peaks were observed.

As shown in Fig. 4a, we designed a special scan mode to improve the density of samples. In such model, side-contour scanning was followed by inside-fill scanning. Contour scanning is a key role to the precision and surface roughness of samples, therefore we chose a spot size of 90 μm , the laser scanning speed of 1400 mm/s and the power of 225 W as side-contour scanning parameters, which are different from the parameters of inside-fill scanning. Such low energy density enables surface smoothness and precision to be improved. As for the inside-fill scanning, high energy density can dominate the mechanical property. In Fig. 4b, SEM image shows scanning tracks and scanning direction. As designed, the edge of strut was formed by contour scanning and the centre was the parallel melt pools formed by laser scanning with specific angle. The reason we chose small hatch distance is that the melt pools can overlap and enables powders to fully melt therefore improve sample density.

Figure 4c shows dendrites morphology within a solidified melt pool track in the X-Z (i.e. build direction) plane. Different types of dendrites and the melt pool boundaries were observed in SEM image. Dendrites with columnar shape were found growing vertically to the melt pool boundaries. And the centre of the melt pool, dendrites with water drop shape were observed. This is similar to the microstructure observed in SLM-processed 17-4 PH steel, where the columnar grains grow from multiple locations in the melt pool boundary and grow toward the centre of the melt pool. Columnar grains have fine-scale grain diameters, although the length of these grains runs through several layers. It is known that metal parts produced by laser-based

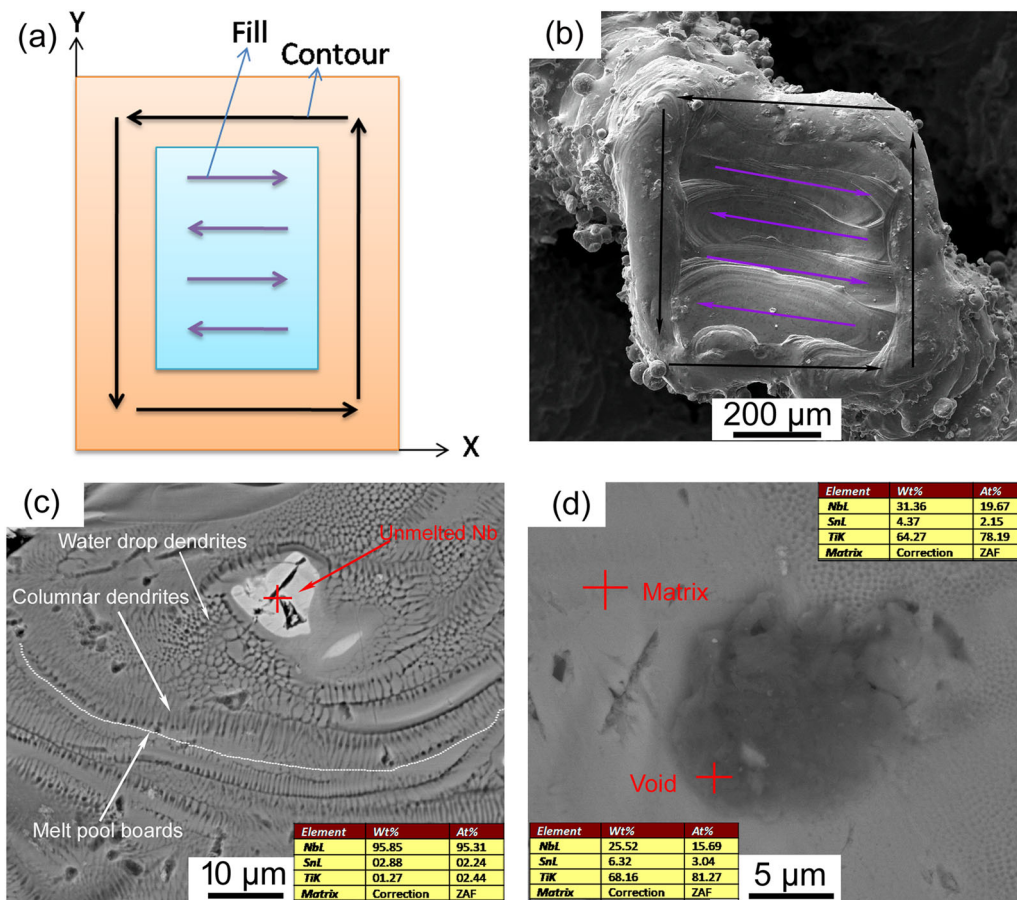


Fig. 4 **a** Designed scanning mode and **b** the real scanning path of sample D3 in SLM processing. SEM micrograph of **c** grains shape in the melt pool and **d** void at X-Z cross-sections (vertical plane) in S2

methods have finer grain sizes than cast or wrought produced parts [30]. Several types of defects were found in SEM image of metallographical samples. In Fig. 4c, the energy dispersive spectrometer (EDS) demonstrated that the main element in the structure with brighter colour is Nb. Because the laser energy density was insufficient to fully melt the Nb powders due to the high melting point (2468 °C) of Nb, some of the Nb particles were unmelted. Besides, unmelted niobium particles have higher thermal conductivity compared to the solid solution, which results in higher temperature gradient in the liquid phase surrounding the niobium particles as heat is dissipated away from the liquid phase faster along the niobium particles [31, 32]. Figure 4d exhibits the morphology of the typical void. According to EDS analysis, the content of Nb elements in that hole was decreased whereas that of Sn increased. Two possible reasons were considered. One is that the evaporation of Sn elements pushed away the melted liquid metal leading to formation of holes [33]. Another is that the holes were formed at where some unmelted Nb particles used to loosely connect to but fell off during metallographic preparation.

3.2 Surface morphologies of porous samples and the balling phenomenon

Figure 5 shows SEM surface morphology of different porous samples. All porous samples show good formability and well correspond to designed CAD models. The uniform strut without surface undulation was observed, as well as no apparent deformation and collapse. As shown in Fig. 5e, contrast to diamond structure, some of holes with badly welded particles were observed at the junction of strut in rhombic dodecahedron structure. Moreover, struts defects were also observed. Besides, we found that many spherical particles adhered to the strut surface in all samples.

Figure 6 shows the details of spherical particles on sample surface under high-resolution SEM. According to EDS analysis, the majority of particles adhering to surface of strut were detected as pure Ti particles, while the content of particles locating at intersection of struts was similar to matrix. The formation of former particles can be attributed to unmelted sintered particles and that of the later thanks to the balling phenomenon. Moreover, these spherical particles affected the structure of surrounding matrix. Figure 6c is the

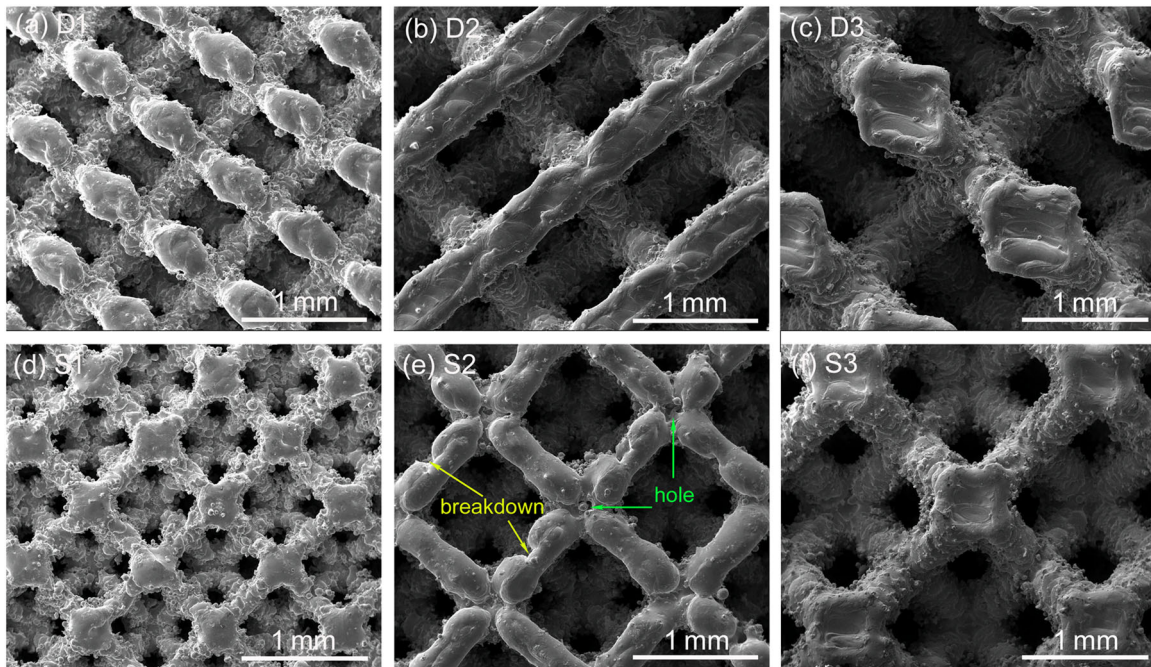


Fig. 5 Surface morphologies of SLM-manufactured porous samples with diamond (a D1, b D2 and c D3) and rhombic dodecahedron (d S1, e S2 and f S3) structure

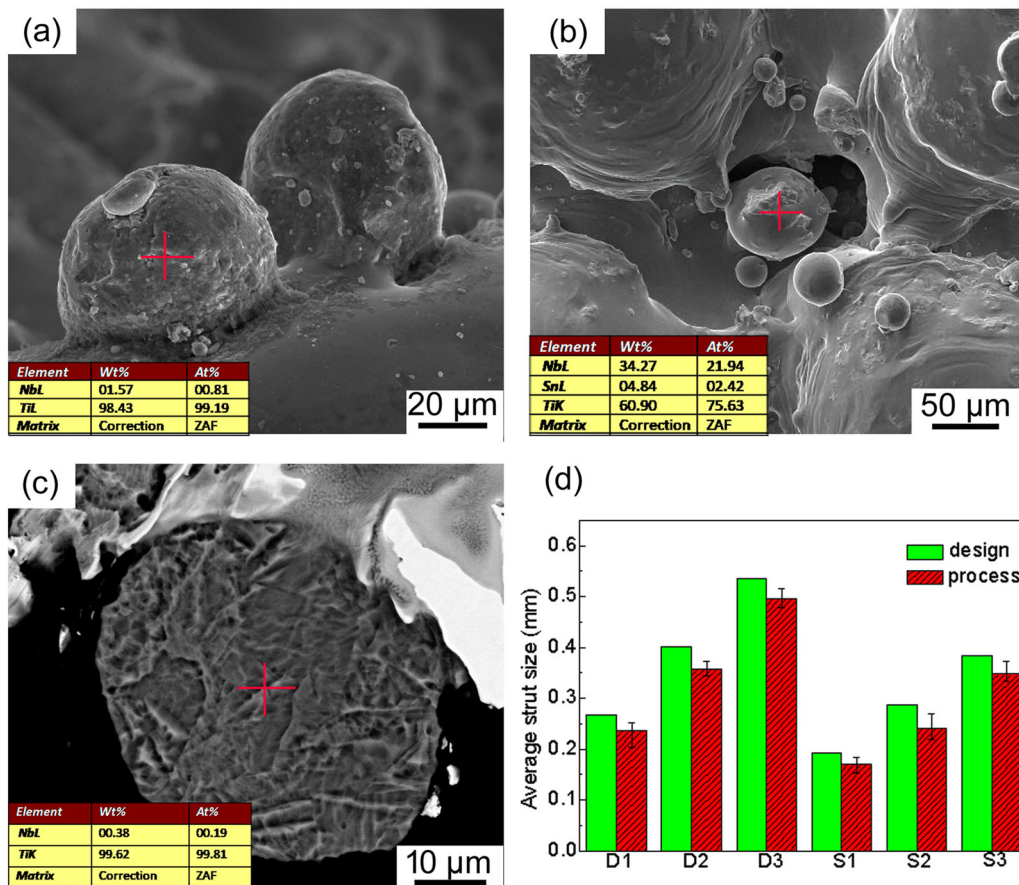


Fig. 6 SEM micrographs of unmelted sintered particles **a** and balling spherical particles **b** in the Ti–33Nb–4Sn alloy. The balling spherical particles in **b** were conducted in the intersection of struts of S2. **c** SEM micrographs of pure Ti particle in the strut edge in D3. **d** The comparison of average strut size between process values and design values

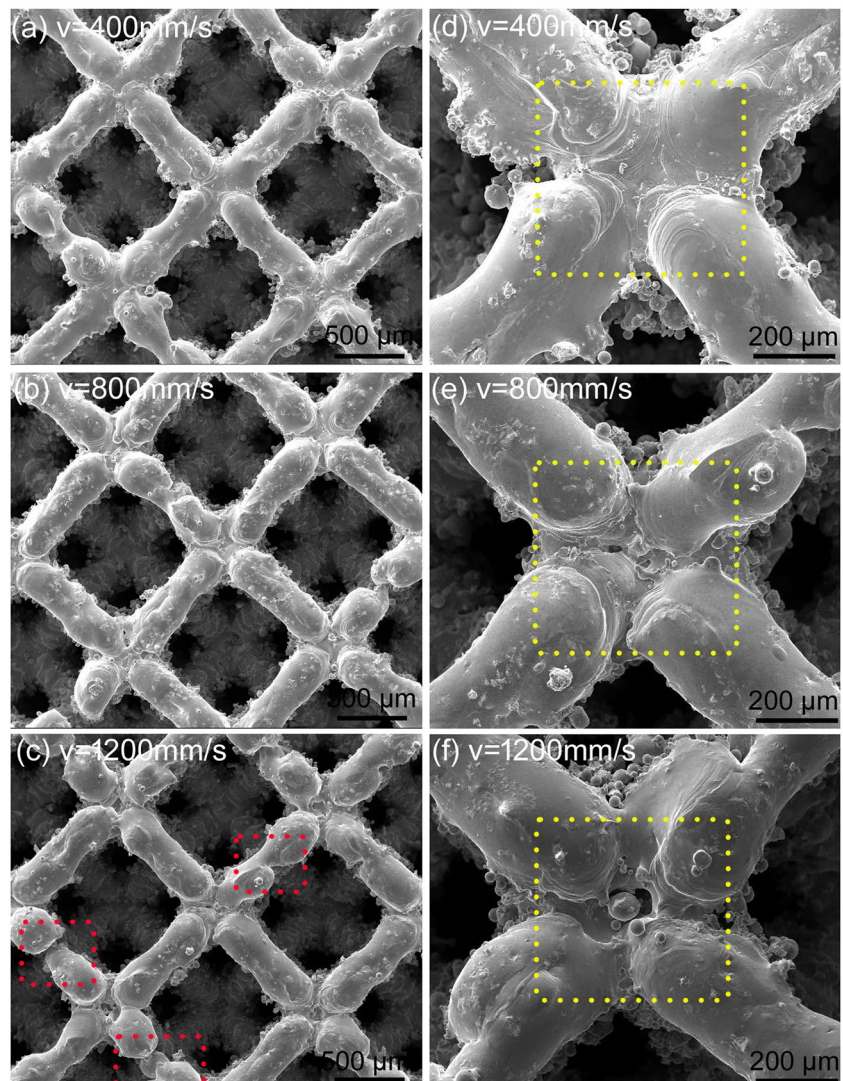
SEM image of spherical particles adhering to the strut edge. Those particles showed typical lamellar structure of α -type Ti and fine dendrite crystals appeared at the connecting part of matrix. Such texture is different from other parts of matrix. Besides, some cracks were observed at that part.

Particles adhering to strut will occupy part of the pores' volume, which would lead to lower real porosity than designed porosity. The rigid cellular plastics method was chosen to measure the real porosity of the scaffolds. For porous samples, when measuring the porosity with the Archimedes methods, water will infiltrate into the pores, which results in lower buoyancy and consequently a relatively higher density. Therefore, in this work, testing of rigid cellular plastics method was considered to measure the porosity. The real porosity of all porous samples was obtained by average of ten times repeated experiment. The results from D1 to S3 were 70.8%, 68.8%, 69.1%, 68.5%, 71.2%, 70.1%, respectively, which are close to the designed porosity of 70%. The reason is considered as contraction of

strut diameter during SLM processing. The volume of contraction was offset by volume of particles. To verify this assumption, we measured strut size in SEM image. All the measure-points locate at smooth surface with few particles and all samples were measured for 10 times. As shown in Fig. 6d, the real strut size was all lower than design strut size. Two possible reasons are considered: one is that the fast cooling speed of SLM leads to contraction of samples, and the second one is the dimensional error of SLM processing [34]. There are few publications about this issue, and this is worthy for further research.

Gu et al. [35] reported the surface of SLM parts existed small particles (about 10 μm), which is ascribed as the second type of balling phenomenon. Such phenomenon can be decreased by increasing energy density (E). Therefore, we investigated the balling phenomenon in the dodecahedron structures with different scanning speeds (v) of 400, 800 and 1200 mm/s. As shown in Fig. 7, the surface morphology was investigated by SEM. There was no obvious

Fig. 7 The low magnification SEM images of spherical particles and struts integrity of the S2 samples fabricated with scanning speeds of **a** 400 mm/s, **b** 800 mm/s and **c** 1200 mm/s. High magnification SEM images of balling phenomenon at the struts intersection with scanning speeds of **d** 400 mm/s, **e** 800 mm/s and **f** 1200 mm/s



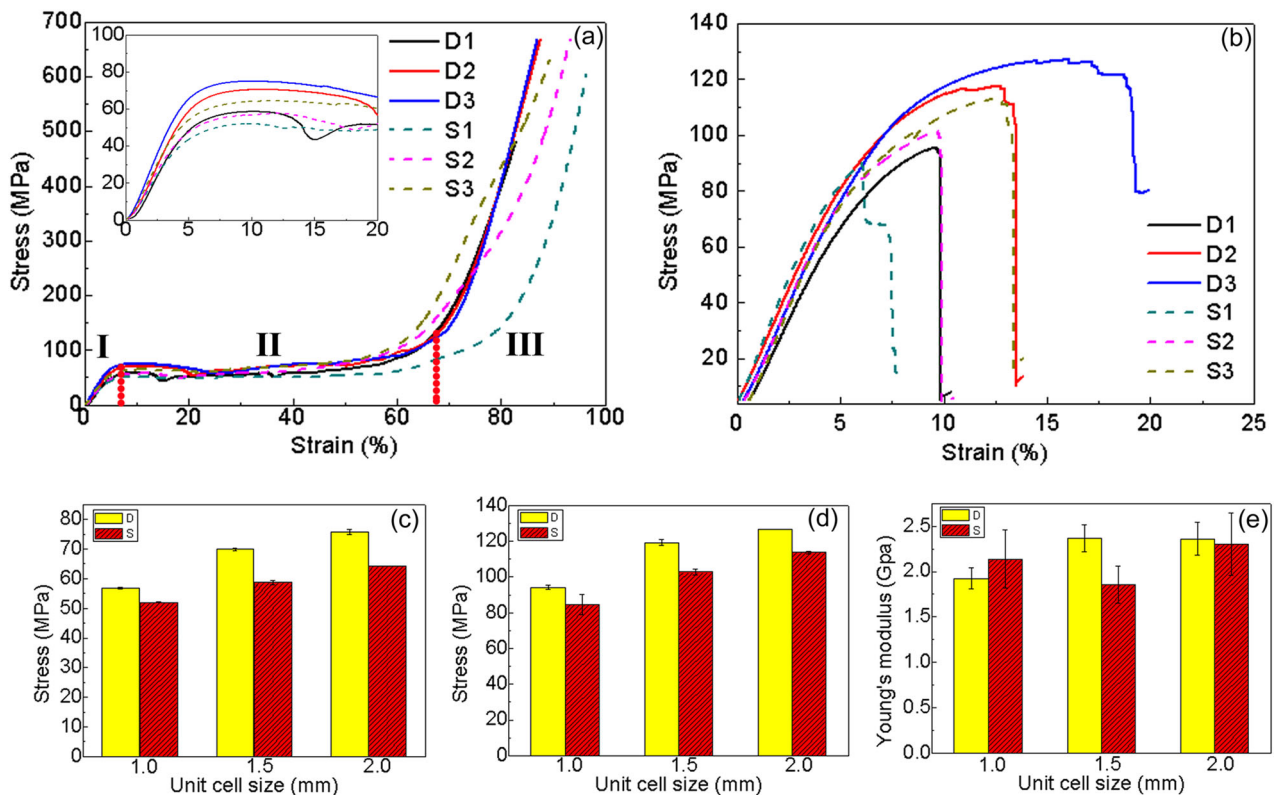


Fig. 8 **a** The typical compressive tests stress-strain curves for all porous samples. **b** The typical bending tests stress-strain curves for all porous samples. The histogram of **c** the compressive strength, **d** the bending strength and **e** the elastic modulus of all Ti-33Nb-4Sn porous samples

difference of strut surface observed between those samples (Fig. 7a–c), which demonstrated that the particles adhering to surface were unmelted sintered particles. However, the strut integrity decreased following decrease of E . The low E results in multiple defects occurring on struts. As for the intersection of strut (Fig. 7d–f), the number of holes increases with the decrease of E , and some spherical particles can be observed inside the holes, which are clear evidence of balling phenomenon.

3.3 Mechanical properties and fracture

The stress-strain curves are shown in Fig. 8a. The curves of all samples were similar, all experiencing three stages. The first stage is the linear elastic portion caused by elastic deformation of strut and only takes small part of the whole curves. In this stage, linear relationship between stress and strain can be observed. The second stage is the constant stress portion. During compressing, metal struts won't immediately connect to each other to achieve the density because of the high porosity. In this stage, samples experience a long-term deformation under a certain stress. Such stress platform is ascribed to the balance between stress decrease caused by holes collapse and stress increase caused by holes densification. The third stage is densification portion. In this stage, density increases following the

increase of strain, and struts of porous sample start to contact with each other. Therefore, the compression to porous samples in this stage, which corresponds to the compression to bulk metal, will lead to a rapid stress increase. As implants, such characteristics of porous samples can act as a buffering to prevent the implants from being broken by external forces. Consequently, it will increase success rate of orthopaedic operation.

As shown in bending curves (Fig. 8b), at first, the stress-strain curves show linear relationship which means the bending of struts. When strain reaches a certain level, stress reaches to a highest point and then dramatically plummets, corresponding to fracture of struts. Following the growth of strain, the S1 sample shows the lowest bending strength of 90 ± 2.2 MPa and D3 exhibits the highest bending strength of 127 ± 0.2 MPa. The small errors of bending strength demonstrate the high repeatability of the experiments. Figure 8c, d indicate the compressive strength and bending strength of porous samples, respectively. The compressive strength and bending strength of porous samples with same structures both increased following the increase of unit cell sizes. As for comparison between those samples with different structure, diamond structure samples always showed better mechanical properties than dodecahedron structure samples with same unit cell size. Results showed that the diamond structure with each unit cell size of 2.0 mm

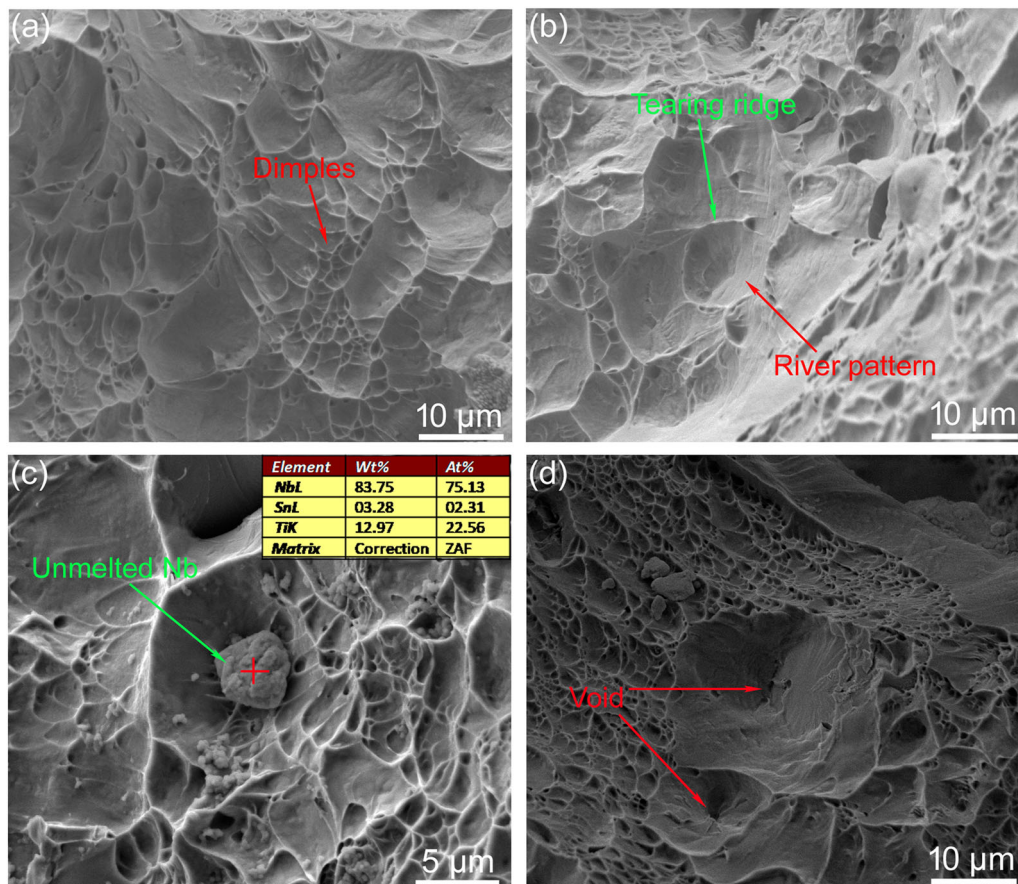


Fig. 9 The fracture morphologies of **a** the tearing dimples in D2, **b** the quasi-cleavage fracture with tearing ridges and river patterns in S3, **c** unmelted Nb particles in D1 and **d** holes in D1

presented the highest compressive strength of 76 ± 0.9 MPa and bending strength of 127 ± 0.2 MPa, which exhibits superior performance than the reported Ti2448 rhombic dodecahedron scaffolds fabricated either by SLM (compressive strength of 50 MPa with porosity of 75% and each unit cell size of 3.33 mm [36]) or EBM (compressive strength of 37 MPa with porosity of 70% and each unit cell size of 2.0 mm [37]).

The elastic modulus of all samples is shown in Fig. 8e. It can be seen that neither unit cell size nor porous structure has significant effects on the value of elastic modulus. All the samples show elastic modulus around 1.8–2.3 GPa. The diamond structure with each unit cell size of 2.0 mm exhibits higher value of 2.3 GPa and the dodecahedron structure with each unit cell size of 1.5 mm exhibits low value of 1.8 GPa. The elastic modulus is an important performance index of biomaterials. The relationship between elastic modulus and porosity can be ascribed to the easy compressibility of pores. Although different pore structure and unit cell size have been selected in this study, all the samples possess a fixed porosity of 70% according to the designed model. Therefore, all the samples show the similar elastic modulus.

The Fig. 9 shows the microscopic morphology of the fracture observed by SEM. It can be seen in Fig. 9a that the microscopic features are some dimples with different sizes and irregular shapes. There were many small dimples distributing between big dimples. In the bending test, the dimples were elongated along the direction of the relatively higher stress, and the tearing dimples were formed under such tear stress. Those elongated dimples were in the shape of parabola. Figure 9b shows a mixing fracture consisting of dimples and cleavage facets. The fracture with river pattern spreads along a certain crystal plane, but it has tearing ridge caused by large plastic deformation. This kind of fracture can be defined as quasi-cleavage fracture, whose river patterns extend from the inside to edge. Such river patterns are short and discontinuous, and the confluence characteristics are not obvious. The tearing ridges, which are petal-like, were visible between facets. It is proposed that the reason of the formation of such fracture is micro-cracks caused by stress concentration. With the increase of stress, cracks expand as step-like way in quasi-cleavage facets to form river patterns. The existence of dislocation and twins leads to serious lattice deformation. Because the directions of cracks in a same grain are different, the expansion of cracks

is difficult. When cracks expand, they will connect with each other by plastic deformation at the edge, which leads to tearing edges.

The fracture of alloys can be divided into three parts: formation, expansion and separation of cracks. As shown in Fig. 9c, d, crack appeared around the unmelted Nb particles and holes. Dislocation loops accumulated around the unmelted Nb particles in Fig. 9c. Being suffered from external force, dislocation will slip, which leads to formation of micropore. Besides, the close connection between Nb particles and matrix can prevent crack from expansion which can cause formation of dimples with bigger size. Therefore, it can improve the ductility. As shown in Fig. 9d, cracks exist inside holes, which lead to plastic deformation. Such plastic deformation can generate river pattern extending from centre of the holes to edge, and consequently decrease the ductility. In general, the fracture of alloys can be considered as ductile fracture, whereas the cleavage facets occurring at the holes can be ascribed to brittle fracture. Therefore, the procedure parameters can be adjusted to prevent defects and consequently improve the ductility.

4 Discussion

4.1 The specific direction and different shapes of dendrites

It is known that SLM manufacturing processes are very complex and highly dynamic, where the thermal and temperature distribution of the melt pool have significant effect on the resulting microstructure. In this work, dendrites with columnar shape were found growing vertically to the melt pool boundaries. At the centre of the melt pool, dendrites with water drop shape were observed (Fig. 4c). Such specific direction depends on orientation growth of crystals which is decided by crystal structure. The Ti–Nb–Sn alloy belongs to near β -type Ti whose crystal structure shows bcc structure. Therefore, the dendrites tend to grow in the $\langle 100 \rangle$ direction [38]. The solidification features of samples are considered to be related to formation of dendrites with different shapes. During fast solidification of SLM samples, grain grows as the speed of interfacial movement after random nucleation. The growth speed of grain relates to undercooling degree and grain size depends on growth condition of dendrite tip. When laser beam hit the sample, melt pool was formed centring on this laser beam. The temperature in the centre of melt pool is usually higher than that at the edge which leads to higher undercooling degree required for solidification of grain locating at the edge of melt pool. Therefore, the grain nucleation occurs preferentially at the edge of melt pool. Liquid-solid interface grows as dendrites following certain direction. When grain

growth reaches to the centre of melt pool where no obvious temperature gradient exists, grain tends to grow as water drop dendrites [31].

4.2 Two kinds of spherical particles

During the SLM build process, the particles appeared not only on sample surface, but also at the intersection of struts (Fig. 6a, b). The formation of those particles can be attributed to unmelted sintered particles and the balling phenomenon respectively. As shown in Fig. 6a, the observed particles are similar to these raw pure titanium particles. When laser beam hits metallic powders to form melt pool, the area surrounding to melt pool generates a heat affected zone, in which temperature is lower than that of melt pool, that produces these half-melted powders. Moreover, the laser beam, in the form of impulse, transforms from some of kinetic energy to surface energy of powders, leading to lots of small-sized particles attached to the strut surface. Furthermore, the angles between struts and build plane are 45° and struts were built on loose powders. Because of the different heat transport between solid struts and powders, powders particles adhere to the surface of struts [39, 40]. Figure 6b shows the particles in locating at intersection of struts, which is ascribed to the surface balling phenomenon. During melting, liquid metals may present two states on solid substrate: spreading around the liquid or congregating to the centre of liquid. The spreading of liquid metals depends on the wettability between liquid metals and solid substrate, as well as the fluidity of liquid pool [41]. If the wettability is bad, powders can hardly spread around the substrate while melting can tend to form a ball [28]. Even though such balling phenomenon increases the surface roughness, it will be detrimental to mechanical property, especially the fatigue strength, due to partial heterogeneities and stress concentration caused by those small particles. Moreover, those particles connect loosely to the surface which means they may be released into biological system causing inflammation [42].

4.3 Mechanical properties comparison between diamond and rhombic dodecahedron porous structures

In compress test, the porosity of all samples was around 70%, but the compress strength of samples with same structure and porosity decreased following the decrease of unit cell size. Because the smaller the struts size, the more sensitive it is to the defects such as Sn segregation, unmelted Nb particles and the balling particles. As for porous materials with different structures, compression test indicated that the compress strength of samples with diamond structure is much higher than that of samples with

dodecahedron structure. According to SEM image in Fig. 5, this is ascribed by holes only appearing at the intersection of struts in dodecahedron structure samples, and some crack at struts was observed. Besides, each joint in diamond structure connects to four struts, while in dodecahedron structure each joint connects to eight struts. Therefore, the joints in dodecahedron structure are suffering more force than that in diamond structures, finally leading to their break. The structure of diamond is formed through SP3 hybridization occurring between one carbon atom and four adjacent carbon atoms. Such dense three dimensional crystal structure is the most stable and firm among natural materials which response to the lower compress strength of dodecahedron structure samples. The same result in bending test compared with compress test can verify such conclusion.

5 Conclusions

In this work, diamond and rhombic dodecahedron structured porous β -type biomedical Ti–33Nb–4Sn scaffolds were fabricated by SLM. The surface morphology, formability and balling phenomenon of the scaffolds were studied. The phase, microstructure and defects characteristics of the SLM-fabricated Ti–33Nb–4Sn alloy were analysed. The mechanical properties of scaffolds with different pore structures and sizes were evaluated. Based on these experiments, the results are summarized as follows.

- (1) Both diamond and rhombic dodecahedron structured Ti–33Nb–4Sn scaffolds showed good formability without apparent deformation and collapse of the struts. Compared with the diamond structure, holes and discontinuities were observed at the intersection of struts of rhombic dodecahedron structure.
- (2) High cooling rate in SLM processing resulted in fast solidification of the alloy, thus fine β phase dendrites were obtained in the Ti–33Nb–4 Sn scaffolds. Columnar dendrites locating at the boundary of melt pool and water drop dendrites locating at the centre of melt pool were demonstrated. The huge difference in melting point of Sn and Nb lead to segregation of Sn and the formation of unmelted Nb particles during solidification. Besides, holes generated by evaporation of Sn were also observed in the alloys.
- (3) Spherical particles loosely adhered to surface were observed at the intersection of struts in rhombic dodecahedron structure, which was attributed to surface balling phenomenon caused by low fluidity and insufficient wettability of liquid metal. This balling phenomenon can be restrained by increasing energy density input in the SLM process.
- (4) Due to the presence of defects such as Sn segregation, unmelted Nb and balling particles in the SLM processed Ti–33Nb–4Sn, both the compressive strength and bending strength of the samples decrease with the decrease of strut sizes. It was demonstrated that diamond structure samples always showed better mechanical properties than dodecahedron structure samples with the same unit cell size. A typical compressive strength of 76 MPa, bending strength of 127 MPa and elastic modulus of 2.3 GPa were obtained in the diamond structured Ti–33Nb–4Sn scaffolds with unit cell size of 2.0 mm.

Acknowledgements The authors would like to acknowledge financial supports from the National Key R&D Program of China (No. 2017YFB0306300), the National Natural Science Foundation of China (No. 51602350), the China Postdoctoral Science Foundation (2017M610505), the Key R&D Program of Hunan Province, China (No. 2016JC2003), the Natural Science Foundation of Hunan Province, China (No. 2018JJ3654) and the fund of State Key Laboratory of Powder Metallurgy, Central South University.

Compliance with ethical standards

Conflict of interest The authors declare that they have no conflict of interest.

Publisher's note: Springer Nature remains neutral with regard to jurisdictional claims in published maps and institutional affiliations.

References

1. Geetha M, Singh AK, Asokamani R, Gogia AK. Ti based biomaterials, the ultimate choice for orthopaedic implants-A review. *Prog Mater Sci.* 2009;54:397–425.
2. Fojt J, Fousova M, Jablonska E, Joska L, Hybasek V, Pruchova E, et al. Corrosion behaviour and cell interaction of Ti–6Al–4V alloy prepared by two techniques of 3D printing. *Mater Sci Eng C.* 2018;93:911–20.
3. Tong J, Bowen CR, Plummer J. Mechanical properties of titanium-based Ti–6Al–4V alloys manufactured by powder bed additive manufacture. *Mater Sci Technol.* 2017;33:138–48.
4. Haghghi SE, Lu H, Jian G, Cao G, Habibi D, Zhang LC. Effect of α' martensite on the microstructure and mechanical properties of beta-type Ti–Fe–Ta alloys. *Mater Des.* 2015;76:47–54.
5. Murr LE, Gaytan S, Ceylan A, Martinez E, Martinez J, Hernandez D, et al. Characterization of titanium aluminide alloy components fabricated by additive manufacturing using electron beam melting. *Acta Mater.* 2010;58:1887–94.
6. Sercombe TB, Xu X, Challis VJ, Green R, Sheng Y, Zhang Z, et al. Failure modes in high strength and stiffness to weight scaffolds produced by selective laser melting. *Mater Des.* 2015;67:501–8.
7. Wang Q, Han CJ, Choma T, Wei QS, Yan CZ, Song B, et al. Effect of Nb content on microstructure, property and in vitro apatite-forming capability of Ti–Nb alloys fabricated via selective laser melting. *Mater Des.* 2017;126:268–77.
8. Liu YJ, Wang HL, Li SJ, Wang SG, Wang WJ, Hou WT, et al. Compressive and fatigue behavior of beta-type titanium porous

- structures fabricated by electron beam melting. *Acta Mater.* 2017;126:58–66.
9. Miura K, Yamada N, Hanada S, Jung T.-K, Itoi E. The bone tissue compatibility of a new Ti–Nb–Sn alloy with a low Young's modulus. *Acta Biomater.* 2011;7:2320–6.
 10. Chang LL, Wang YD, Ren Y. In-situ investigation of stress-induced martensitic transformation in Ti–Nb binary alloys with low Young's modulus. *Mater Sci Eng A.* 2016;651:442–8.
 11. Moraes PE, Contieri RJ, Lopes ES, Robin A, Caram R. Effects of Sn addition on the microstructure, mechanical properties and corrosion behavior of Ti–Nb–Sn alloys. *Mater Charact.* 2014;96:273–81.
 12. Pina VG, Dalmau A, Devesa F, Amigo V, Munoz AI. Tribocorrosion behavior of beta titanium biomedical alloys in phosphate buffer saline solution. *J Mech Behav Biomed Mater.* 2015;46:59–68.
 13. Griza S, de Souza Sa DHG, Batista WW, de Blas JCG, Pereira LC. Microstructure and mechanical properties of hot rolled TiNbSn alloys. *Mater Des.* 2014;56:200–8.
 14. Matsumoto H, Watanabe S, Hanada S. Beta TiNbSn alloys with low Young's modulus and high strength. *Mater Trans.* 2005;46:1070–8.
 15. Salvador CA, Lopes ES, Ospina CA, Caram R. Orthorhombic martensite formation upon aging in a Ti–30Nb–4Sn alloy. *Mater Chem Phys.* 2016;183:238–46.
 16. Guo S, Meng QK, Zhao XQ, Wei QM, Xu HB. Design and fabrication of a metastable beta-type titanium alloy with ultralow elastic modulus and high strength. *Sci Rep.* 2015;5:14688
 17. Chen W, Chen C, Lin YC, Zi XH, Cheng XF, Zhang XY, et al. Controlling the microstructure and mechanical properties of a metastable β titanium alloy by selective laser melting. *Mater Sci Eng A.* 2018;726:240–50.
 18. Zhou CC, Deng CY, Chen XN, Zhao XF, Chen Y, Fan YJ, et al. Mechanical and biological properties of the micro-/nano-grain functionally graded hydroxyapatite bioceramics for bone tissue engineering. *J Mech Behav Biomed Mater.* 2015;48:1–11.
 19. Wang Z, Wang C, Li C, Qin Y, Zhong L, Chen B, et al. Analysis of factors influencing bone in growth into three-dimensional printed porous metal scaffolds: a review. *J Alloy Compd.* 2017;717:271–85.
 20. Cattalini J, Hoppe A, Pishbin F, Roether J, Boccaccini A, Lucangioli S, et al. Novel nanocomposite biomaterials with controlled copper/calcium release capability for bone tissue engineering multifunctional scaffolds. *J R Soc Interface.* 2015;12:20150509
 21. Chia-Ying L, Tobias W, Frank LM, Scott JH. Structural and mechanical evaluations of a topology optimized titanium interbody fusion cage fabricated by selective laser melting process. *J Biomed Mater Res A.* 2007;10:31231
 22. Tan XP, Tan YJ, Chow CSL, Tor SB, Yeong WY. Metallic powder-bed based 3D printing of cellular scaffolds for orthopaedic implants: A state-of-the-art review on manufacturing, topological design, mechanical properties and biocompatibility. *Mater Sci Eng C.* 2017;76:1328–43.
 23. Carter LN, Wang X, Read N, Khan R, Aristizabal M, Essa K, Attallah MM. Process optimisation of selective laser melting using energy density model for nickel based superalloys. *Mater Sci Technol.* 2016;32:657–61.
 24. Kempen K, Thijs L, Van Humbeeck J, Kruth J.-P. Processing AlSi10Mg by selective laser melting: parameter optimisation and material characterization. *Mater Sci Technol.* 2015;31:917–23.
 25. Zhou ZX, Cunningham E, Lennon A, McCarthy HO, Buchanan F, Dunne N. Development of three-dimensional printing polymer-ceramic scaffolds with enhanced compressive properties and tuneable resorption. *Mater Sci Eng C.* 2018;93:975–86.
 26. Zhuravleva K, Bonisch M, Prashanth KG, Hempel U, Helth A, Gemming T, et al. Production of porous beta-type Ti–40Nb alloy for biomedical applications: comparison of selective laser melting and hot pressing. *Materials.* 2013;6:5700–12.
 27. Zhang BQ, Pei X, Zhou CC, Fan YJ, Jiang Q, Ronca A, et al. The biomimetic design and 3D printing of customized mechanical properties porous Ti6Al4V scaffold for load-bearing bone reconstruction. *Mater Des.* 2018;152:30–9.
 28. Sallica-Leva E, Jardini AL, Fogagnolo JB. Microstructure and mechanical behavior of porous Ti-6Al-4V parts obtained by selective laser melting. *J Mech Behav Biomed Mater.* 2013;26:98–108.
 29. Liu YJ, Li XP, Zhang LC, Sercombe TB. Processing and properties of topologically optimized biomedical Ti–24Nb–4Zr–8Sn scaffolds manufactured by selective laser melting. *Mater Sci Eng A.* 2015;642:268–78.
 30. Rafi HK, Pal D, Patil N, Starr TL, Stucker BE. Microstructure and mechanical behavior of 17-4 precipitation hardenable steel processed by selective laser melting. *J Mater Eng Preform.* 2014;23:4421–8.
 31. Sing SL, Wiria FE, Yeong WF. Selective laser melting of titanium alloy with 50 wt% tantalum: Microstructure and mechanical properties. *J Alloy Compd.* 2016;660:461–70.
 32. Loh LE, Chua CK, Yeong WY, Song J, Mapar M, Sing SL, et al. Numerical investigation and an effective modelling on the selective laser melting (SLM) process with aluminium alloy 6061. *Int J Heat Mass Transf.* 2015;80:288–300.
 33. Semak V, Matsunawa A. The role of recoil pressure in energy balance during laser materials processing. *J Phys D Appl Phys.* 1998;30:2541–52.
 34. Silva DN, De Oliveira MG, Meurer MI, Da Silva JVL, Santa-Barbara A. Dimensional error in selective laser sintering and 3D-printing of models for craniomaxillary anatomy reconstruction. *J Cranio Maxill Surg.* 2008;36:443–9.
 35. Gu DD, Shen YF. Balling phenomena indirect laser sintering of stainless steel powder: Metallurgical mechanisms and control methods. *Mater Des.* 2009;30:2903–10.
 36. Liu YJ, Li SJ, Wang HL, Hou WT, Hao YL, Yang R, et al. Microstructure, defects and mechanical behavior of beta-type titanium porous structures manufactured by electron beam melting and selective laser melting. *Acta Mater.* 2016;113:56–67.
 37. Liu YJ, Li SJ, Hou WT, Wang SG, Hao YL, Yang R, et al. Electron Beam Melted Beta-type Ti–24Nb–4Zr–8Sn Porous Structures With High Strength-to-Modulus Ratio. *J Mater Sci Technol.* 2016;32:505–8.
 38. Rappaz M, Gandin CA. Probabilistic modeling of microstructure formation in solidification processes. *Acta Met Mater.* 1993;41:345–60.
 39. Mullen L, Stamp RC, Fox P, Jones E, Ngo C, Sutcliffe CJ. Selective Laser Melting: A Unit Cell Approach for the Manufacture of Porous, Titanium, Bone-In-Growth Constructs, Suitable for Orthopedic Applications. II. Randomized Structures. *J Biomed Mater Res B Appl Biomater.* 2009;92B:178–88.
 40. Pyka G, Kerckhofs G, Van Bael S, Moesen M, Loeckx D, Schrooten J, et al. Non-destructive characterization of the influence of surface modification on the morphology and mechanical behavior of rapid prototyped Ti6Al4V bone tissue engineering scaffolds. *Moscow: European Conference for Non-Destructive Testing (ECNDT);* 2010.
 41. Gu DD, Shen YF. Balling phenomena during direct sintering of multicomponent Cu based metal powder. *J Alloy Compd.* 2007;432:163–6.
 42. Hollander DR, Von Walter M, Wirtz T, Sellei R, Schmidt-Rohlfing B, Paar O, et al. Structural, mechanical and invitro characterization of individually structured Ti–6Al–4V produced by direct laser forming. *Biomaterials.* 2006;27:955–63.